Extreme Mechanics Letters 72 (2024) 102239

Contents lists available at ScienceDirect

Extreme Mechanics Letters

journal homepage: www.elsevier.com/locate/eml

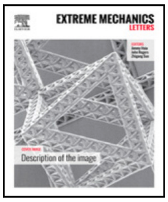

Hopping potential wells and gait switching in a fish-like robot with a bistable tail

Prashanth Chivkula, Colin Rodwell, Phanindra Tallapragada *

Clemson University Department of Mechanical Engineering, 216 South Palmetto Blvd, Clemson, 29634, SC, USA

ARTICLE INFO

MSC:
0000
1111

Keywords:
Bistability
Robotic swimming

ABSTRACT

Fish outperform current underwater robots in speed, agility, and efficiency of locomotion, in part due to their flexible appendages that are capable of rich combinations of modes of motion. In fish-like robots, actuating many different modes of oscillation of tails or fins can become a challenge. This paper presents a highly underactuated (with a single actuator) fish-like robot with a bistable tail that features a double-well elastic potential. Oscillations of such a tail depend on the frequency and amplitude of excitation, and tuning the frequency–amplitude can produce controllable oscillations in different modes leading to different gaits of the robot. This robot design is inspired by recent work on underactuated flexible swimming robots driven by a single rotor. The oscillations of the rotor can propel and steer the robot, but saturation of the rotor makes performing long turns challenging. This paper demonstrates that by adding geometric bistability to the flexible tail, turns can be performed by controllably exciting single-well oscillations in the tail, while exciting double-well oscillations of the tail produces average straight-line motion. The findings of this paper go beyond the application to a narrow class of fish-like robots. More broadly we have demonstrated the use of periodic excitation to produce bistable response that generate different gaits including a steering gait. The mechanics demonstrated here show the feasibility of applications to other mobile soft robots.

1. Introduction

The development of robots designed to swim effectively on and under the surface of the water has become a major frontier of robotics. This is motivated by the numerous current and emerging applications including environmental monitoring, search, inspection and security of underwater structures and infrastructure and numerous other military applications. Robotics researchers have sought inspiration from aquatic animals to design swimming robots. However, despite significant advancements, modern underwater robots continue to be outperformed by fish in aspects such as agility, energy efficiency, and stealth [1]. In an attempt to gain these characteristics, several robots have been designed that replicate the morphology and gaits of fish and other biological swimmers. Designs for fish-like robots include those that are assemblages of rigid links actuated by motors which imitate the motion of tails and fins [2], motor-driven flexible links [3,4], elongated snake and eel-like robots [5,6]. While this approach generates superficially similar swimming in specific straight line motion and turning gaits, the underlying dynamics are very different, as the mechanics of fish locomotion are likely underactuated [7–9]. Fish swimming is strongly influenced by the body's flexibility and the ability to modulate flexibility of the body or the tail can activate different modes of undulations or oscillations. The unactuated or free degrees of freedom offer advantages to many facets of swimming, such as energy harvesting from fluid disturbances, sensing, and agility. These effects are prominent enough that a fully underactuated (dead) fish was found to self-orient and swim upstream in a water tunnel in the wake of a blunt obstacle [10]. Mimicking this underactuation in swimming robots in a manner that can modulate the stiffness or excite different modes of tail oscillations has the potential to confer these advantages while simultaneously reducing the number and cost of actuators required.

There are many different approaches to designing underactuated underwater robots. In some designs, a tail with flexible components is directly actuated to generate motion [3,4,11–13]. In other recent swimming robots [14–19], an internal rotor imposes rotational motion to the main body of the robot, which in turn excites oscillations in the attached flexible tail. The internal rotor driven robots have simple designs and are very modular with passive tails that can be changed to produce different swimming characteristics without a redesign of the robot. While these rotor driven robots have been found to achieve straight-line speeds comparable to their tail driven counterparts, their agility has so far been substantially lower. This results from different turning mechanisms: in a directly tail-driven robot, biasing the direction of the tail to the left or right will tend to induce a turn due

---

* Corresponding author.
E-mail address: ptallap@clemson.edu (P. Tallapragada).

https://doi.org/10.1016/j.eml.2024.102239
Received 21 January 2024; Received in revised form 13 August 2024; Accepted 30 September 2024

to a rudder-like effect. By contrast, internal rotor driven robots can generate a strong impulsive turning force by accelerating the rotor in the direction opposite the turn. While this is effective for short, fast turns, the limited angular velocity that the motor can generate applies a constraint to the amount of time the rotor can be accelerated, and thus a constraint on the distance of turning that is achievable. Further, decelerating the rotor back to its rest state causes typically undesired turning motion in the direction opposite to the previous turn.

In this work, we demonstrate an approach to allow turning in underactuated rotor-driven robots without adding an additional degree of actuation by introducing geometric nonlinearity to the flexible tail, resulting in bistability. The bistability is configured to enable symmetrical stable configurations corresponding to the tail bending either left or right, with an unstable center position. Impulsive forcing of the rotor can snap the tail into the desired configuration, and high-frequency oscillations of the rotor result in off-center flapping motion that induces a turn. However, lower-frequency oscillations induce tail oscillations that symmetrically transit between both stable configurations, enabling straight-line motion. The experimental results with such a bistable tail show different modes of turning motions, which roughly correspond to the ratchet turns, gliding turns and powered turns that are observed in agile fish [20]. The bistable mechanism enables the effective stiffness of the tail to vary mimicking the ability of fish to modulate their flexibility to enhance swimming.

Bistable mechanisms have many applications in robotics; they have been used in multiple space applications [21], in jumping robots [22], in aerial robots and robotic grippers such as in [23,24] or in morphing origami structures in [25]. In aquatic robots, [26] shows the use of a flexural tensegrity snapping bistable tail for propelling a toy boat while [27] uses a bistable shape memory polymer muscles that use temperature changes for actuating paddles on an aquatic robot for propulsion. More recent papers such as [28] have demonstrated fast snap-through instabilities in soft robots with pneumatic actuation and mechanical springs and [29] demonstrated the use of snap through instabilities in a hairpin mechanism to generates undulatory in swimming. What make the results in this paper novel compared to such applications of bistability in robotics, is that periodic forcing is used to trigger frequency–amplitude dependent bistable responses that generate two unique gaits. Beyond the simplicity of mechanical design of the robot in this paper bistability is used to generate different gaits and steering action and not merely fast motion by snap-through instabilities such as in [28,29]. The overall design of the bistable mechanism is simple but leverages nonlinear dynamic response to periodic forcing. Such a combination of mechanics with modular design can pave the way for robots with multiwell potentials that can exploit multistability to achieve superior agility, speed and efficiency.

2. Underactuated fish-like robots propelled by an internal rotor

Fish-like propulsion can be achieved by a robot without the presence of active tails or fins by using the sinusoidal motion of an internal rotor. Such locomotion has been theoretically modeled in [15,30,31] and experimentally demonstrated in [15–19]. The principle behind the locomotion of fish-shaped body by an internal rotor, as illustrated in Fig. 1, is as follows. When a spinning rotor (with angular velocity Ω_r) inside a body that is submerged has an angular acceleration due to the application of a torque via a motor, an equal and opposite counter torque is exerted on the swimmer. This counter torque induces a rotation Ω of the swimmer in the opposite direction. The effective inertia tensor of a body in water is different from that of the same body in a vacuum due to the mass of fluid moving with the body, and it depends on the direction of its velocity (V_1, V_2) in the body frame $X_b - Y_b$; this is encapsulated in the so called added inertia tensor. In an ideal inviscid fluid these displacements over each cycle of rotation of the internal rotor would sum to zero and the robot would have no net displacement. But in a real fluid with viscosity, as the body counter-rotates in response to the rotor, vorticity is created on the boundary and released from the body, usually at the sharp edges, illustrated in the simulated vortex by the red and blue filled circles in Fig. 1. This vorticity and the resulting pressure field creates a propulsive thrust, resulting in a net displacement of the robot. Periodic oscillations of the internal rotor can create a practically smooth motion of the robot as shown in [16,18,19,32].

The turning ability of such rotor driven rigid body robots is generally inferior to their tail-driven counterparts, with a large turning radius and slow rate of turning as shown in [16]. When an impulsive torque is applied on the robot via the internal rotor, the body begins to turn but quickly encounters hydrodynamic resistance to this turning motion. The internal rotor in this case spins in one direction with either constant or increasing angular speed. To improve this turning motion, rotor-driven robots with passive tails have been investigated. It has been shown in [17] that a passive tail improves turning motion by creating vorticity (clockwise or counterclockwise) that produces a hydrodynamic moment that favors the turn. Similarly in [19] it was shown by the application of Lighthill's slender body theory [33], that sufficiently long flexible tails not only help in making fast turns, but also improve thrust. Nevertheless, even for robots with passive tails whose turning is produced by impulsive torques, during the turn, the tail remains deflected but does not create further propulsion to move the robot further along the curved path. The body conforms into a steady curved configuration, with no tail oscillations necessary to continue to propel the body. As a result, this type of turning is transient, with both the angular and translational velocity of the body rapidly decaying. Additionally, when these turns are complete and the rotor speed is brought back to zero, it results in an undesired turn opposite the direction of the previous one. This turning back motion can be reduced through more complex control strategies such as in [18,34,35], but cannot be fully eliminated. Such control strategies if successful will require an accurate model of swimming and steering under unsteady torque inputs which is a challenge. In a similar vein, tracking curved paths with a reference speed requires complex control strategies [18,36]. Robots with bistable tails that can controllably oscillate in two different modes and can be triggered to switch between these modes with minimal control effort will have overcome many of the challenges imposed by the mechanics of the fluid–structure interaction.

3. Design of a robot with a bistable tail

A bistable passive tail can be realized through a simple assembly of prestretched springs connected to a passive tail plate. The robot shown in Fig. 2(a)–(b) consists of the main body referred to as the 'head' with an extruded hydrofoil shape, with chord length 150 mm, maximum thickness 65 mm, and extruded height 85 mm. The tail seen in Fig. 2(b) is a sheet of PETG plastic (Youngs modulus $E = 2.01 \times 10^9$ N/m^2) with a thickness of 0.64 mm, height of 85 mm, and length of 100 mm. The geometry of the sheet is such that it has an angled trailing edge to optimize thrust. This geometry of the tail was found to yield the maximum self propelled swimming speed in [37]. Springs of stiffness $K = 484$ N/m and rest length 34 mm are mounted to both sides of the tail. As the tail bends to the side, the extension of the spring on the outward side of the bend increases only slightly, while the extension of the spring on the inside of the bend decreases significantly. Because the elastic potential of the tail itself is symmetrical about its straight line position, its gradient with respect to deflection must be 0 when straight, but the potential energy of the spring has a non-zero gradient with respect to tail deflection angle. This guarantees the straight tail configuration to be a local maximum of the mechanical potential and ensures the existence of minima to both sides, which correspond to a left and right deflected positions as seen in Fig. 2(c). A schematic of the robot's geometry is shown in Fig. 2(f). Inside the extruded shell, an Antigravity T-series 380 Kv brushless electric motor is installed

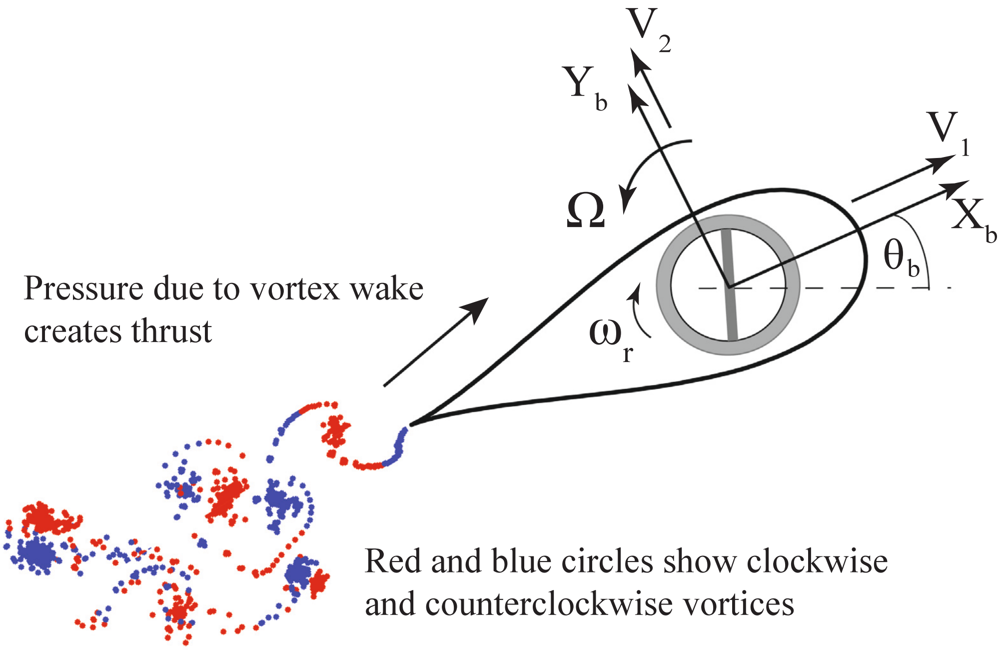

Fig. 1. Thrust generation on a fish-shaped body (a Joukowski hydrofoil) due to the sinusoidal motion of an internal rotor. (For interpretation of the references to colour in this figure legend, the reader is referred to the web version of this article.)

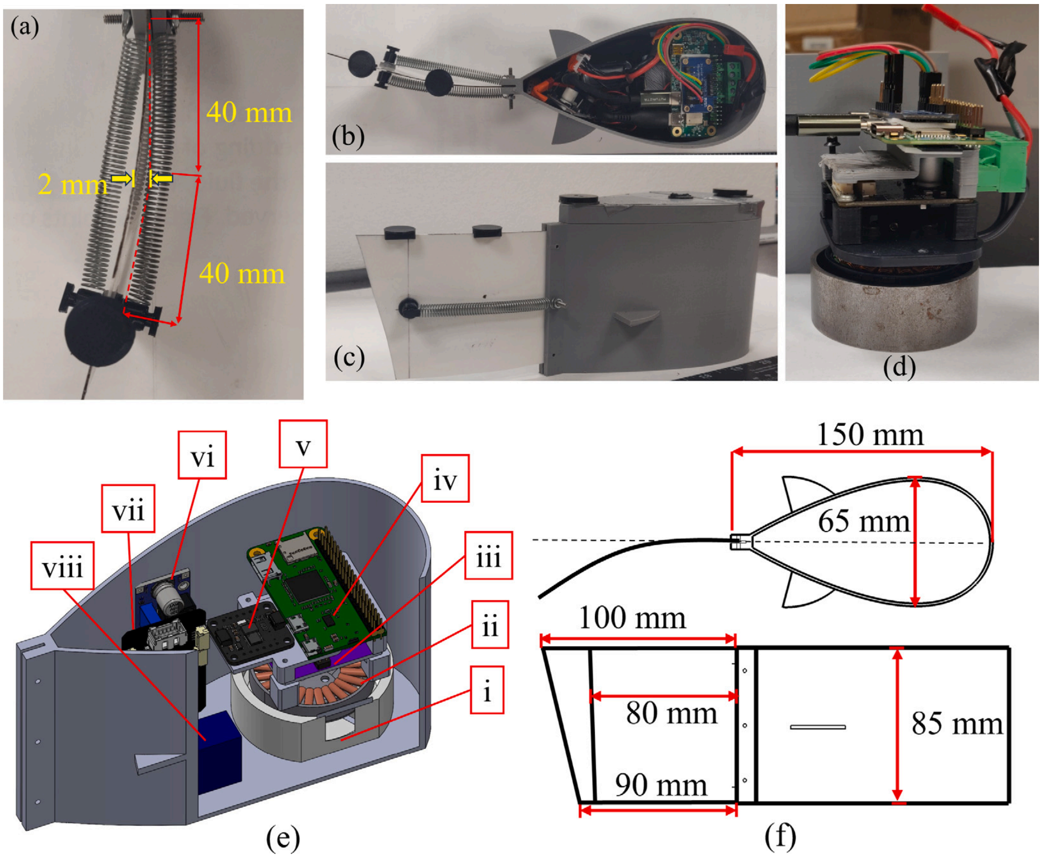

Fig. 2. (a) shows the tail of the robot in one of the stable equilibrium positions due to the two pre-tensioned springs on the left and right side of the tail. (b) shows the top view of the robot along with the internal electronics. (c) is the side view of the robot and the four black markers are used for tracking the robot by the camera. (d) shows the assembled rotor module with components stacked together. (e) shows a representative CAD section view of the robot labeled with all the component descriptions in Table 1. (f) shows the geometry of the hydrofoil with its chord length and thickness. It also shows the unbent angled-trailing edge geometry and attached dimensions of the tail when inserted 10 mm into the slit of the main body.

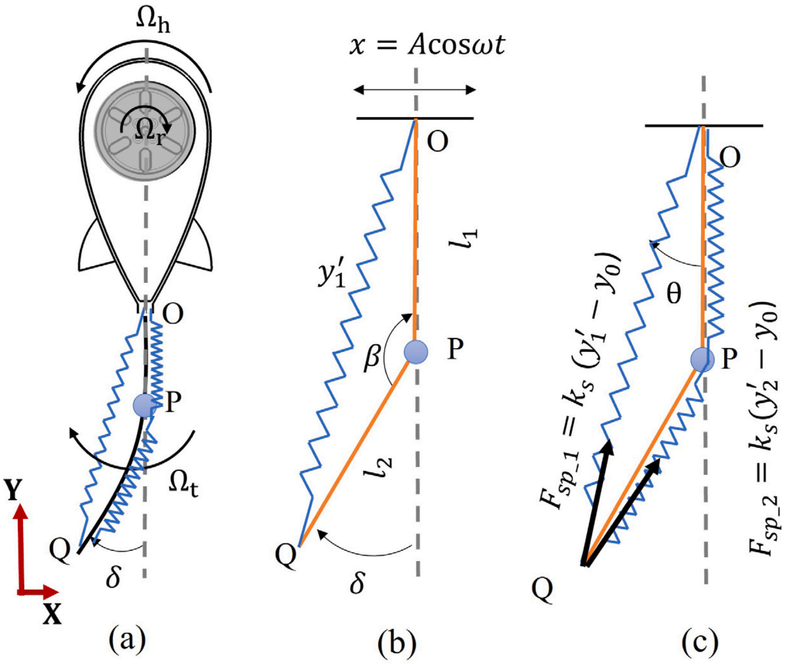

Fig. 3. (a) shows a schematic of the robot actuated by angular velocity Ω_r which results in the oscillations of the tail with angular velocity Ω_t about one of the stable configurations due to the spring (b) shows a lumped parameter model of the flexible sheet as two links OP and PQ of lengths l_1 and l_2 respectively pinned to the hydrofoil at O. The position of point O undergoes lateral (sway) oscillations $x = A\cos\Omega t$. Two pretensioned springs of length of $y_1{}'$ and $y_2{}'$ pinned at O and Q on either side of the links. (c) shows the forces due to the springs with rest length y_o acting on the sheet and where θ is the angle made by the left spring with respect to the tail where $F_s = F_{sp_1} - F_{sp_2}$.

Table 1
Component specifications.

No.	Component	Specification
i	Rotor	AISI 1045 Carbon Steel
ii	Motor	T-motor MN4006 KV380
iii	Motor driver	Tinymovr R5
iv	Single board computer	Raspberry Pi Zero W
v	IMU	Adafruit LSM9DS0 9 DOF
vi	Voltage regulator	LM2596
vii	CAN-USB adapter	CANine USB-CAN adapter
viii	Batteries	3.7 V (5S), 400 mAh

horizontally with an rotor of mass 106 g mounted directly below. The motor is driven by a Tinymovr R5.1, which is in turn powered by 5 cells of 3.7 V, 400 mAh Li-Po batteries, which are connected in series and mounted towards the tail end of the body. A Raspberry Pi-Zero controls the Tinymovr and saves data from an LSM9DS0 IMU, mounted horizontally.

4. Analytical model for a bistable tail

An analysis of a simplified model of a swimming robot with a flexible bistable tail architecture motivates the possibility of multiple gaits. Fig. 3(a) shows a schematic of the rotor-driven robot in one of the stable configurations. To focus on the dynamics of the tail, we assume a simplified model where the kinematics of the main body of the robot are kinematically prescribed. This simplification is motivated by the following observations. When the internal rotor oscillates periodically, the main body of the robot undergoes yaw oscillations and sway(lateral) oscillations was demonstrated in [14,16,38]. Motivated by these observations, we assume the connection point O sways laterally as $x = A\cos\omega t$ with the body having no other motion. A body frame collocated at the center of mass of the main body is chosen. The tail deflects as shown in Fig. 3(b) and in the physical model as in Fig. 2(a)–(b). As these figures show, while the tail plate is a flexible continuum it can be essentially modeled consisting of two rigid links l_1 and l_2, with a spring of length y' connecting their ends. The segments OP and PQ have lengths l_1 and l_2 respectively as shown in Fig. 3(b)–(c). The tail segment is OP is modeled as being fixed and always in the same alignment. Experiments described in Section 5 justify this as the deflection angle of OP is always less than 0.05 rad. The angle δ defines the angle between the links l_2 and l_1. As l_1 is considered as a fixed link, the angle δ is as shown in Fig. 3. The length of the links are such that $l_1 = l_2 = L$.

$$V(\delta) = \frac{1}{2}k_s(2L^2\cos\delta - 2y_0\sqrt{2L^2 + 2L^2\cos\delta}) + \frac{1}{2}k_f L^2\sin^2\delta. \tag{1}$$

The function $V(\delta)$ is a double well potential with one extrema at $\delta = 0$. Another pair of extrema, when they exist, are given by the roots of the equation $\frac{k_f}{k_s}\cos\delta = 1 - \frac{y_o}{2L\cos\frac{\delta}{2}}$. The second pair of fixed points exist only if $\frac{k_f}{k_s}$ is sufficiently small, i.e. the stiffness of the system is dominated by the stiffness of the springs over the stiffness of the cantilever beam. As described in the Appendix, the parameters of the system are such that this condition is satisfied. A further analysis of the equation of motion will demonstrate that the double well potential combined with viscous damping and oscillations of the support yield a forced Duffing oscillator. After some straightforward calculations (see Appendix for details) the equation for deflection of the tail can be written as

$$\left(I + \frac{1}{4}mL^2\right)\ddot{\delta} + c\dot{\delta} + k_s L^2\sin\delta\left(\frac{y_o}{L\sqrt{2(1+\cos\delta)}} - 1\right) + \frac{1}{2}k_f L^2\sin 2\delta = -\frac{1}{2}mL\cos\delta\ddot{x} \tag{2}$$

where c is the coefficient of damping. We set $mR^2 = I + \frac{1}{4}mL^2$ and $\ddot{x}$ with $-\omega^2 A_s\cos\omega t$, divide throughout by the inertia mR^2. In order to further simplify the equation and reduce the number of parameters we set $A = \frac{A_s L}{2R^2}$, $\zeta = \frac{c}{mR^2}$, $\Omega_1^2 = k_s\frac{L^2}{mR^2}$ and $\Omega_2^2 = \frac{k_f L^2}{2mR^2}$ and note that $\sqrt{2(1+\cos\delta)} = 2\cos\frac{\delta}{2}$. With these observation the equation of motion can be simplified to

$$\ddot{\delta} + \zeta\dot{\delta} + \Omega_1^2\sin\delta\left(\frac{y_o}{2L\cos\frac{\delta}{2}} - 1\right) + \Omega_2^2\sin 2\delta = \omega^2 A\cos\delta\cos\omega t \tag{3}$$

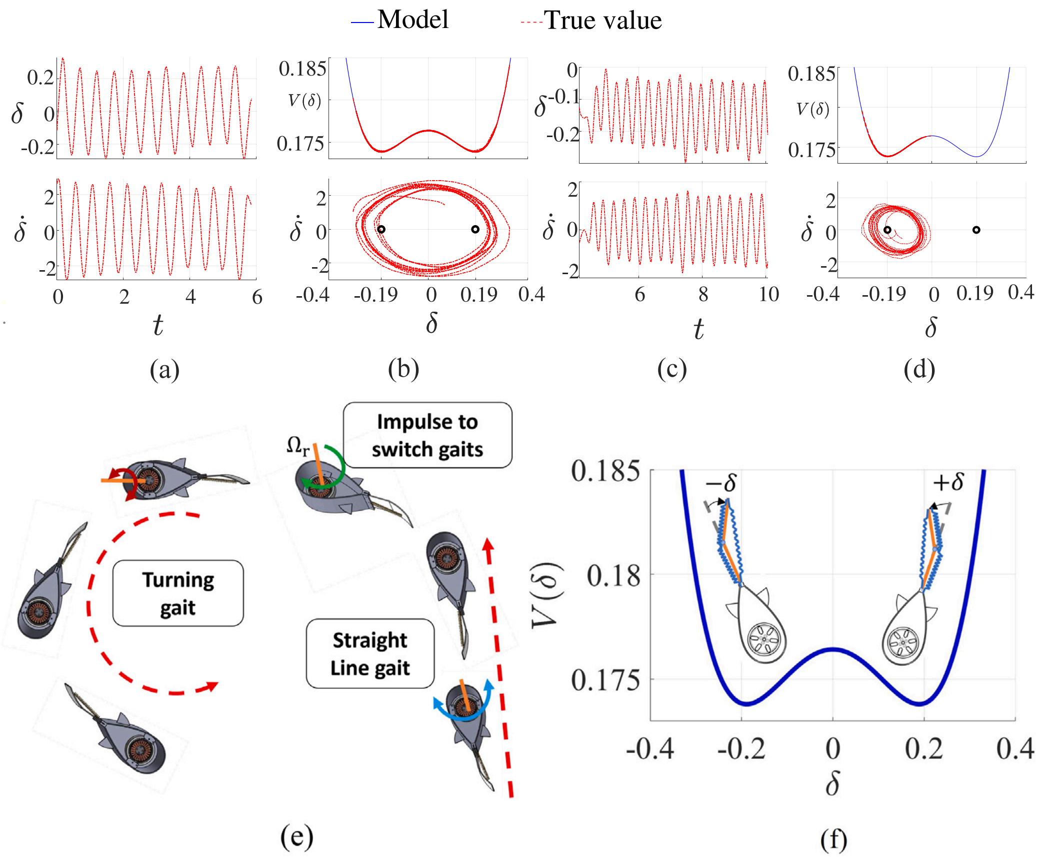

Fig. 4. (a) shows tail angle δ of the robot oscillating about a zero mean and angular velocity $\dot{\delta}$ as a result of inter-well oscillations. (b) shows the double well oscillations of the tail around the two fixed points (in black) $\delta = \pm 0.20$ rad. (c) shows δ oscillating about non-zero mean i.e the fixed point $\delta = -0.20$ and resulting angular velocity during single-well oscillations (d) shows the tail in the left potential well and the corresponding phase portrait. (e) shows a robot the performs inter-well oscillations as result of a low frequency and high amplitude input Ω_r (blue arrow), an impulse (green arrow) to the rotor to switch gaits and then high frequency and low amplitude (red arrow) input to the rotor generates single-well oscillations of the tail about the deflected equilibrium which leads to turning in the counter-clockwise direction. (f) shows the double well potential of the tail with the two stable deflected equilibrium positions of the tail. (For interpretation of the references to colour in this figure legend, the reader is referred to the web version of this article.)

Approximating $\frac{1}{\cos\delta/2} \approx 1 + \frac{1}{8}\delta^2$ and $\sin\delta \approx \delta$ and noting that $\frac{y_0}{2L} < 1$, one obtains the equation of a Duffing oscillator

$$\ddot{\delta} + \zeta\dot{\delta} + \left(2\Omega_2^2 - \Omega_1^2 + \Omega_1^2\frac{y_o}{2L}\right)\delta + \Omega_1^2\frac{y_o}{16L}\delta^3 = \omega^2 A\cos\delta\cos\omega t \tag{4}$$

For periodically forced Duffing oscillator, there exists a forcing amplitude–frequency that causes the oscillations of the tail to stay in a single-well or hop between the two wells (inter well oscillations), see for instance [39]. When the tail oscillates in only one potential well, i.e. about a deflected equilibrium, an asymmetric (in the body frame) lift force and moment are produced on the body leading to a turning motion. When the tail performs inter well oscillations, the lift force is on the average zero and only a thrust is produced leading to average straight line motion. Oscillations in left potential well versus the right potential well lead to turning motion in opposite directions. This analysis and hypothesis are based only on a qualitative analysis of the bistability of the tail, the frequency–amplitude dependence of response that can expected in such a system, but without a quantitative analysis of thrust and turning moment. The hypothesis is tested via experiments.

5. Experimental results

All the experiments were performed in a 6 ft by 8 ft pool. The bottom of the pool has square grid lines measuring 1 inch × 1 inch. Numerical data from the experiment is derived from the encoder embedded on the Tinymovr, the onboard IMU, and the video recorded by the overhead camera. The data from the IMU and encoder are recorded by the Raspberry pi at a rate of 10 Hz. The overhead camera records videos at 60 frames/s. The video from the camera is later post-processed using Tracker-physics video analysis tool and is used to track the position of four markers on the robot which are positioned on the head and tail. Each of these frames are calibrated using the grid at the bottom of the pool. These frames are then used to determine body kinematics, such as the angle of the tail relative to the main body, which is then used to calculate the tail angular velocity through forward finite differences. The encoder keeps track of the angular velocity of the rotor as it gives information about forcing on the body.

We performed three sets of experiments to measure the robot's kinematics in three different motions : straight line motion, turning clockwise and turning counter clockwise. We find through experiments that an input amplitude frequency combination of $A_r = 150$ rad/s and $f = 1.9$ Hz produces inter-well oscillations. Holding the frequency constant at $f = 1.9$ Hz and increasing the amplitude of the input produces larger amplitude inter-well tail oscillations. The first set of experiments use the input amplitude–frequency combination of $A_r =$ 180 rad/s and $f = 1.9$ Hz, that is above the threshold for inter-well oscillations, average straight line motion is generated. Decreasing the input amplitude or increasing the input frequency is seen to produce single well oscillations. For example at input frequency $f = 3$ Hz, for input amplitudes less than 100 rad/s produce single-well oscillations as shown in Fig. 4(a)–(b), with the angle δ varying periodically with nearly zero mean. The next set of experiments is to test turning motion of the robot from a stand still. To generate this turning gait the tail needs to perform oscillations about a deflected equilibrium point. This

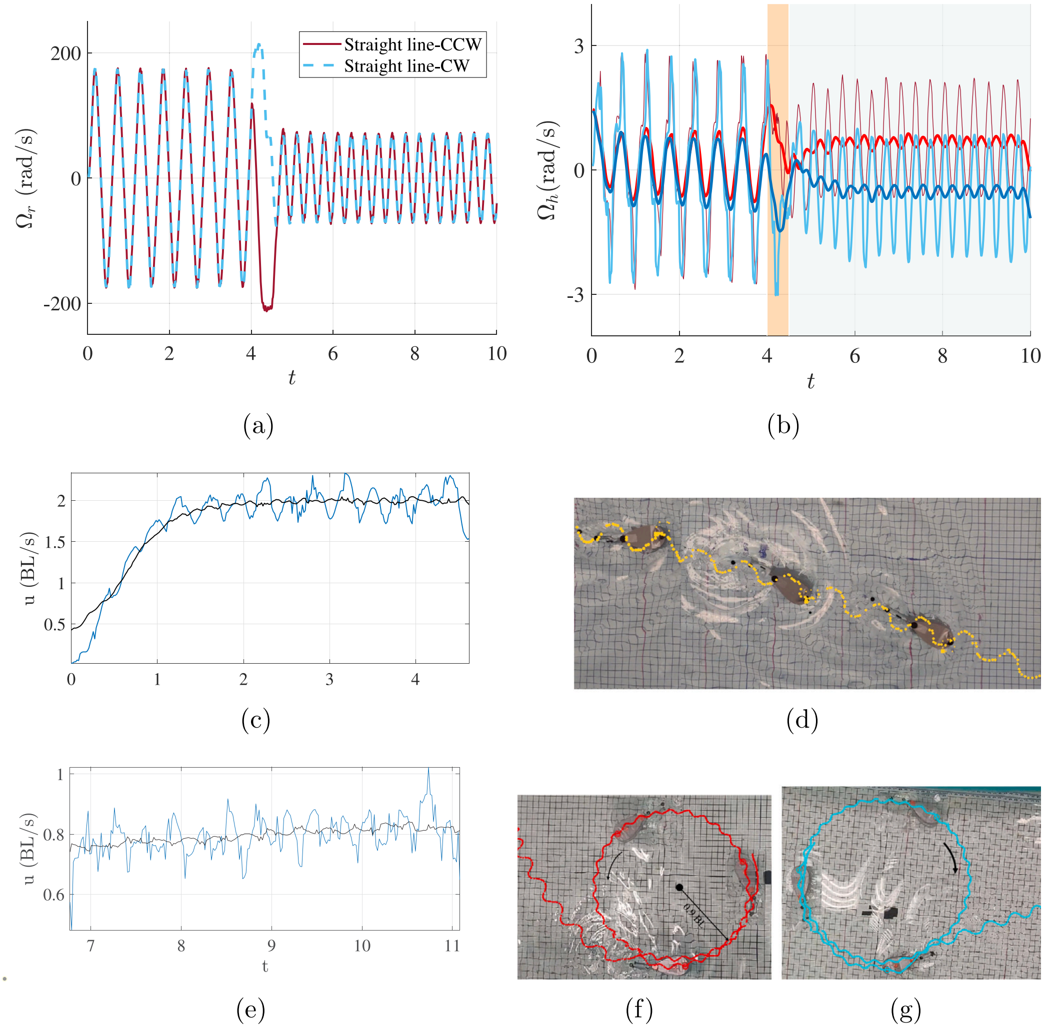

(a) (b) (c) (d) (e) (f) (g)

Fig. 5. (a) shows rotor angular velocity input Ω_r with a high amplitude of 180 rad/s and low frequency of 1.9 Hz which results in inter-well oscillations from $t = 0$ to t = 4.0, an impulse applied between $t = 4$ and $t \leq 4.5$ and Low amplitude of 80 rad/s, high frequency of 3 Hz from $t > 4.5$ (b) shows the resulting head oscillations which oscillate about zero mean for from $t = 0$ to $t = 4$ (white region) where the robot is in straight line gait. At $t = 4$ an impulsive rotor motion occurs and a gait transition occurs (orange region). The head moves and in the direction of turn caused due to the impulse and for $t > 4.5$ shows the head oscillating about a non-zero mean that corresponds to turning gait. (For interpretation of the references to colour in this figure legend, the reader is referred to the web version of this article.)

is done by giving an input of $A_r = 70$ rad/s and $f = 3$ Hz to the rotor. This generates a turning gait in clockwise or counterclockwise motion depending on which initial equilibrium point the tail is deflected to. Fig. 4(c)–(d) shows the results of the tail oscillating in the left potential well, with the tail angle δ, having a mean value less than zero. The oscillation amplitude for both δ and $(\dot{\delta})$ is lower than the corresponding amplitudes for inter-well oscillations. The maximum frequency amplitude combination for the tail to perform single-well oscillations is $A_r = 100$ rad/s and $f = 3$ Hz.

The third set of experiments is to test the ability of the robot to generate both gaits. A prescribed control scheme of the robot is developed such that it performs inter-well oscillations for 4 s using a rotor angular velocity input of $A_r = 180$ rad/s and $f = 1.9$ Hz. As all the control is prescribed and do not receive feedback about which well the tail is in to execute a particular turn, an impulse in the direction of the desired turn is specified for 0.5 s and then the robot transitions to single well oscillations by giving an input of $A_r = 70$ rad/s and $f = 3$ Hz. The entire sequence of prescribed control inputs is shown in Fig. 4(e). In summary the robot has a straight line gait due to the inter-well oscillations of the tail when it receives a low frequency and high amplitude rotor input and has a turning gait due to single oscillations of the tail when it receives low amplitude and high frequency input to the rotor. Fig. 5 (and the supplementary video) shows snapshots of a sequence of these two gaits in an experiment. The rotor initially performs low frequency, high amplitude oscillations, as shown in Fig. 5(a) for the first 4 seconds resulting in inter-well tail oscillations (Fig. 5(b)) and average straight line motion shown in Fig. 5(d), with the average longitudinal velocity reaching about 2 body lengths per second as shown in Fig. 5(c). At $t = 4$ s, and the balanced rotor performs a fast impulsive turn and then resumes sinusoidal oscillations again with a high frequency and low amplitude as shown in Fig. 5(a). Data from two cases is shown, one where the rotor has an impulsive clockwise turn (dashed blue line) and one where the rotor has an impulsive counterclockwise turn (solid red line). This results in the tail deflecting to the left or right and oscillating in the respective potential well resulting in a turning angular velocity for the main body as shown in Fig. 5(b). The longitudinal velocity of the robot decreases to about 0.8 body lengths per second but the robot executes a turning motion as shown in Fig. 5(f)–(g), either in the clockwise or counterclockwise direction. Since the single well oscillations are sustained for about 5 seconds the robot moves along a nearly circular path of radius 0.9 body lengths.

The other two cases which include high-frequency and high amplitude and low frequency and low amplitude angular velocity of the rotor are also tested. For the first case, the highest frequency for a high amplitude that could be tested is 3 Hz. This resulted in fast straight line motion and a top speed of 2.1 BL/s. The second scenario of low frequency and low amplitude still generates a slow turning gait; however for very low frequency of input (less than 1.0 Hz) significant tail oscillations cannot be sustained due to the high hydrodynamic damping.

6. Conclusion

Underactuated swimming robots can achieve different gaits and motion characteristics by exploiting bistable tails. In this paper we have presented the design of a swimming robot that posses only one degree of actuator and has a bistable tail. We demonstrated with experiments and a simplified theoretical model that depending on the frequency and amplitude of the internal oscillations of the actuator the bistable tail can perform either inter-well or single well oscillations and impulsive torques by the same actuator can result in a hop between the potential wells. To our knowledge this is the first paper where the frequency–amplitude combination of a single periodic control input can exploit a bistable mechanism in a swimming robot to produce different gaits. The significance of the results in the paper go beyond the specific type or morphology of the robot. It has usually been difficult to incorporate bistable mechanisms in swimming robots because of the increased mechanical complexity that is required to switch between different stable equilibria and exploit the qualitatively different dynamics. The results in this paper show that such switches can be made easily and different dynamics selected without increasing the mechanical complexity purely by manipulating the frequency–amplitude of actuation. Future work can be expected to lead to improved modeling, parameter estimation and closed loop control algorithm for path tracking.

CRediT authorship contribution statement

Prashanth Chivkula: Writing – original draft, Software, Methodology, Formal analysis, Data curation. **Colin Rodwell:** Writing – original draft, Visualization, Software, Methodology, Investigation, Formal analysis, Data curation. **Phanindra Tallapragada:** Writing – review & editing, Writing – original draft, Project administration, Investigation, Funding acquisition, Formal analysis, Conceptualization.

Declaration of competing interest

The authors declare the following financial interests/personal relationships which may be considered as potential competing interests: Phanindra Tallapragada reports financial support was provided by National Science Foundation. Phanindra Tallapragada reports financial support was provided by Office of Naval Research. If there are other authors, they declare that they have no known competing financial interests or personal relationships that could have appeared to influence the work reported in this paper.

Acknowledgments

This work was supported by grant 13204704 from the Office of Naval Research and the National Science Foundation grant 2021612.

Appendix A

The Lagrangian of the link PQ can be written as: $\mathcal{L} = \frac{1}{2}\dot{q}^T\mathcal{M}(q)\dot{q} - \mathcal{V}(\delta)$, where $\mathcal{M}$ represents the mass matrix and $\mathcal{V}(\delta)$ represents the elastic potential energy of the system and the kinetic energy $\mathcal{T}(q,\dot{q}) = \frac{1}{2}\dot{q}^T\mathcal{M}(q)\dot{q}$ of the system can be written as:

$$\mathcal{T}(q,\dot{q}) = \frac{1}{2}m(\dot{x}^2 + \dot{x}\dot{\delta}L\cos\delta + \frac{1}{4}\dot{\delta}^2L^2) + \frac{1}{2}I\dot{\delta}^2$$

where m represents the mass of link l_2 and I its centroidal moment of inertia. The mass m and moment of inertia I both include added hydrodynamic inertia. Since link l_1 is fixed relative to the base of the tail we ignore the kinetic energy of this link. The potential energy of the system results from stiffness in both the springs k_s and the flexural tail stiffness k_f. The potential energy due to the springs can be written as $\frac{1}{2}k_s(y_1{}' - y_o)^2$ and $\frac{1}{2}k_s(y_2{}' - y_o)^2$ where y_o is the rest length of the spring when in either of the two deflected positions excluding the effect of flexural stiffness of the sheet. The lengths $y_1{}'$ and $y_2{}'$ are of the two springs when in the left deflected position. Thus the total potential energy of the system can be written as $V(\delta) = V_s(\delta) + V_f(\delta)$, where V_s is the potential energy due to the springs and the V_f is from flexural stiffness of the thin plate. The elastic potential is, $V_s = \frac{1}{2}k_s(y_1{}' - y_o)^2 + \frac{1}{2}k_s(y_2{}' - y_o)^2$ and from the geometry shown in Fig. 3(c), using the law of cosines, $(y_1')^2 = 2L^2 + 2L^2\cos\delta$. The length of the other spring $y_2' = 2L$. Substituting these and ignoring constant terms, we find the potential energy of the springs, V_s, is

$$V_s(\delta) = \frac{1}{2}k_s(2L^2\cos\delta - 2y_0\sqrt{2L^2 + 2L^2\cos\delta}). \tag{5}$$

The tail which is a thin plate essentially behaves as a cantilever beam with small in-plane bending. The net force F_s to due to both the springs act at point Q, which is at a distance of $a = 80$ mm from the support, while the tail length itself, denoted by L_o varies uniformly along the depth between 100 mm and 90 mm as shown in Fig. 2(f). The tip deflection of the beam due to the point force at Q is given by, $x_f = \frac{Pa^2(3L-a)}{6EI_p}$ where E the Young's modulus of the beam and I_p the area moment of inertia of the cross section of the beam. From this an approximate stiffness of the lumped parameter flexural spring can be obtained as $k_f = \frac{6EI_p}{a^2(3L_o-a)}$. The Youngs modulus of the PETG is 2.01×10^5 to 2.1×10^5 N/cm^2. Choosing the effective length of the cantilever to be $L_o = 9.5$ cm gives $k_f = 0.151$ N/cm^2 and choosing the effective length of the cantilever to be $L_o = 0.9$ gives $k_f = 0.141$ N/cm^2. An alternative lumped parameter stiffness can be obtained using a strain energy calculation. The elastic strain energy in the cantilever beam is given by $V_f = \int_0^{L_o}\frac{M^2}{2EI}dy$, where the bending moment $M = -F_s(a-y)$ for a point load F_s applied at distance of a from the support. This integral can be expressed in terms of elastic strain energy stored in the beam is $V_f = \frac{1}{2}k_fL^2\sin^2\delta$ where $k_f = \frac{36EI(a^2L_o+L_o^3-aL_o^2)}{a^4(3L_o-a)^2}$. Choosing the effective length of the cantilever to be $L_o = 9.5$ cm gives $0.128 \leq k_f \leq 0.134$ N/cm^2 for $2.01\times10^5 \leq E \leq 2.01\times10^5$ N/cm^2 and choosing the effective length of the cantilever to be $L_o = 0.9$ gives $0.129 \leq k_f \leq 0.135$ N/cm^2 for $2.01\times10^5 \leq E \leq 2.01\times10^5$ N/cm^2. The potential function (1) has a double well potential for all $0 \leq k_f < 1.645$ N/cm^2 and the system loses bistability for $k_f > 1.645$ N/cm^2. The potential function is plotted in Fig. 6 for three representative values of k_f. The approximate values of k_f calculated using different approaches all lie in the range where the potential function has a double well. We choose a value of $k_f = 1.42$ N/cm^2 that is in the middle of the range of the estimates of the lumped parameter stiffness.

We consider a viscous damping modeled by Rayleigh dissipation function as $\mathcal{R} = \frac{1}{2}c\dot{\delta}^2$ with damping coefficient c. The Euler–Lagrange equations can then be written in the form

$$\frac{d}{dt}\left(\frac{\partial\mathcal{L}}{\partial\dot{q}_i}\right) - \frac{\partial\mathcal{L}}{\partial q_i} + \frac{\partial\mathcal{R}}{\partial q_i} = 0.$$

$$\left(I + \frac{1}{4}mL^2\right)\ddot{\delta} + c\dot{\delta} + k_sL^2\sin\delta\left(\frac{y_o}{L\sqrt{2(1+\cos\delta)}} - 1\right) + \frac{1}{2}k_fL^2\sin 2\delta$$
$$= -\frac{1}{2}mL\cos\delta\ddot{x}$$

Appendix B. Supplementary data

Supplementary material related to this article can be found online at https://doi.org/10.1016/j.eml.2024.102239.

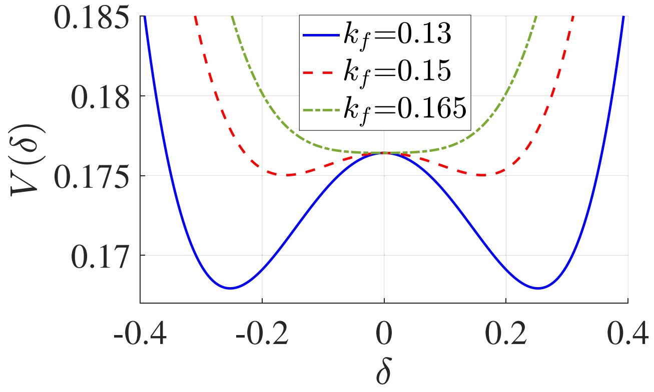

Fig. 6. Potential functions for three representative values of k_f. For $k_f \geq 0.1645$ the potential function has only a single extrema.

Data availability

Data will be made available on request.

References

[1] A. Raj, A. Thakur, Fish-inspired robots: design, sensing, actuation, and autonomy—A review of research, Bioinspir. Biomim. 11 (3) (2016) 031001.

[2] M.S. Triantafyllou, G. Triantafyllou, An efficient swimming machine, Sci. Am. 272 (3) (1995) 64.

[3] J. Zhu, C. White, D.K. Wainwright, V. Di Santo, G.V. Lauder, H. Bart-Smith, Tuna robotics: A high-frequency experimental platform exploring the performance space of swimming fishes, Science Robotics 4 (34) (2019) 4615.

[4] C.H. White, G.V. Lauder, H. Bart-Smith, Tunabot flex: a tuna-inspired robot with body flexibility improves high-performance swimming, Bioinspiration Biomim. 16 (2) (2021) 026019.

[5] E. Kelasidi, P. Liljeback, K.Y. Pettersen, J.T. Gravdahl, Innovation in underwater robots: Biologically inspired swimming snake robots, IEEE Robot. Autom. Mag. 23 (1) (2016) 44–62.

[6] R. Thandiackal, K. Melo, L. Paez, J. Herault, T. Kano, K. Akiyama, F. Boyer, D. Ryczko, A. Ishiguro, A.J. Ijspeert, Emergence of robust self-organized undulatory swimming based on local hydrodynamic force sensing, Sci. Robot. 6 (57) (2021) eabf6354.

[7] F. Fish, G. Lauder, Passive and active flow control by swimming fishes and mammals, Annu. Rev. Fluid Mech. 38 (1) (2006) 193–224.

[8] E.D. Tytell, M.C. Leftwich, C.Y. Hsu, B.E. Griffith, A.H. Cohen, A.J. Smits, C. Hamlet, L.J. Fauci, Role of body stiffness in undulatory swimming: Insights from robotic and computational models, Phys. Rev. Fluids 1 (2016) 073202.

[9] Y.E. Jimenez, K.N. Lucas, J.H. Long, E.D. Tytell, Flexibility is a hidden axis of biomechanical diversity in fishes, J. Exp. Biol. 226 (2023) 10754.

[10] D. Beal, F. Hover, M. Triantafyllou, J. Liao, G. Lauder, Passive propulsion in vortex wakes, J. Fluid Mech. 549 (2006) 385–402.

[11] Z. Chen, S. Shatara, X. Tan, Modeling of biomimetic robotic fish propelled by an ionic polymer metal composite caudal fin., IEEE/ASME Trans. Mechatronics 15 (3) (2010) 448–459.

[12] J. Shintake, V. Cacucciolo, H. Shea, D. Floreano, Soft biomimetic fish robot made of dielectric elastomer actuators, Soft Robotics 5 (4) (2018) 466–474.

[13] A.D. Marchese, C.D. Onal, D. Rus, Autonomous soft robotic fish capable of escape maneuvers using fluidic elastomer actuators, Soft Robotics 1 (1) (2014) 75–87.

[14] M.J. Fairchild, P.M. Hassing, S.D. Kelly, P. Pujari, P. Tallapragada, Single-input planar navigation via proportional heading control exploiting nonholonomic mechanics and vortex shedding, in: Proceedings of the ASME Dynamic Systems and Control Conference, 2011.

[15] P. Tallapragada, A swimming robot with an internal rotor as a nonholonomic system, in: Proceedings of the American Control Conference, 2015.

[16] B. Pollard, P. Tallapragada, An aquatic robot propelled by an internal rotor, IEEE/ASME Trans. Mechatronics 22 (2) (2017) 931–939.

[17] B. Pollard, P. Tallapragada, Passive appendages improve the maneuverability of fish-like robots, IEEE/ASME Trans. Mechatronics 24 (4) (2019) 1586–1596.

[18] B.A. Free, J. Lee, D.A. Paley, Bioinspired pursuit with a swimming robot using feedback control of an internal rotor, Bioinspir. Biomim. 15 (3) (2020) 035005.

[19] A. Wiens, Slender elastic swimmers : kinematics, dynamics, and robotic applications (Ph.D. thesis), Massachusetts Institute OF Technology, Department of Mechanical Engineering, 2020.

[20] A.M. Downs, A. Kolpas, B.A. Block, F.E. Fish, Multiple behaviors for turning performance of Pacific bluefin tuna (thunnus orientalis)., J. Exp. Biol. 226 (4) (2023) 244144.

[21] S.A. Zirbel, K.A. Tolman, B.P. Trease, L.L. Howell, Bistable mechanisms for space applications, PLoS One 11 (12) (2016) e0168218.

[22] Y. Sun, J. Wang, C. Sung, Repeated jumping with the rebound: Self-righting jumping robot leveraging bistable origami-inspired design, in: 2022 International Conference on Robotics and Automation, ICRA, IEEE, 2022, pp. 7189–7195.

[23] H. Zhang, J. Sun, J. Zhao, Compliant bistable gripper for aerial perching and grasping, in: 2019 International Conference on Robotics and Automation, ICRA, IEEE, 2019, pp. 1248–1253.

[24] X. Li, J. McWilliams, M. Li, C. Sung, C. Jiang, Soft hybrid aerial vehicle via bistable mechanism, in: 2021 IEEE International Conference on Robotics and Automation, ICRA, IEEE, 2021, pp. 7107–7113.

[25] S. Sadeghi, S. Li, Dynamic folding of origami by exploiting asymmetric bi-stability, Extreme Mech. Lett. 40 (2020) 100958.

[26] C. Boni, P.M. Reis, G. Royer-Carfagni, Flexural-tensegrity snapping tails for bio-inspired propulsion in fluids, Extreme Mech. Lett. 56 (2022) 101853.

[27] T. Chen, O.R. Bilal, K. Shea, C. Daraio, Harnessing bistability for directional propulsion of soft, untethered robots, Proc. Natl. Acad. Sci. 115 (22) (2018) 5698–5702.

[28] Y. Tang, Y. Chi, J. Sun, T.H. Huang, O.H. Maghsoudi, A. Spence, H. Su, J. Yin, Leveraging elastic instabilities for amplified performance: Spine-inspired high-speed and high-force soft robots, Sci. Adv. 6 (9) (2020).

[29] Z. Xiong, Y. Su, H. Lipson, Fast untethered soft robotic crawler with elastic instability, in: 2023 IEEE International Conference on Robotics and Automation, ICRA, 2023, pp. 2606–2612.

[30] P. Tallapragada, S.D. Kelly, Reduced-order modeling of propulsive vortex shedding from a free pitching hydrofoil with an internal rotor, in: Proceedings of the 2013 American Control Conference, 2013.

[31] P. Tallapragada, S.D. Kelly, Self-propulsion of free solid bodies with internal rotors via localized singular vortex shedding in planar ideal fluids, Eur. Phys. J. Spec. Top. (2015).

[32] B. Pollard, P. Tallapragada, Passive appendages improve the maneuverability of fish-like robots, IEEE/ASME Trans. Mechatronics (2019).

[33] M.J. Lighthill, Hydrodynamics of aquatic animal propulsion, Annu. Rev. Fluid Mech. 1 (1969) 413–446.

[34] G. Knizhnik, P. DeZonia, M. Yim, Pauses provide effective control for an underactuated oscillating swimming robot, IEEE Robot. Autom. Lett. 5 (4) (2020) 5075–5080.

[35] G. Knizhnik, M. Yim, Thrust direction control of an underactuated oscillating swimming robot, in: 2021 IEEE/RSJ International Conference on Intelligent Robots and Systems, IROS, IEEE, 2021, pp. 8665–8670.

[36] C. Rodwell, P. Tallapragada, Physics-informed reinforcement learning for motion control of a fish-like swimming robot, Sci. Rep. 13 (1) (2023) 10754.

[37] S. Alben, C. Witt, T.V. Baker, E. Anderson, G.V. Lauder, Dynamics of freely swimming flexible foils, Phys. Fluids 24 (5) (2012) 051901.

[38] B. Pollard, V. Fedonyuk, P. Tallapragada, Swimming on limit cycles with nonholonomic constraints, Nonlinear Dynam. 97 (4) (2019) 2453–2468.

[39] A.H. Nayfeh, Introduction to Perturbation techniques, Wiley-VCH, 1993.